

IMPRINTS OF ELECTRON-POSITRON WINDS ON THE MULTI-WAVELENGTH AFTERGLOWS OF GAMMA-RAY BURSTS

J. J. Geng^{1,2}, X. F. Wu^{3,4}, Y. F. Huang^{1,2}, L. Li^{5,6} and Z. G. Dai^{1,2}

ABSTRACT

Optical re-brightenings in the afterglows of some gamma-ray bursts (GRBs) are unexpected within the framework of the simple external shock model. While it has been suggested that the central engines of some GRBs are newly born magnetars, we aim to relate the behaviors of magnetars to the optical re-brightenings. A newly born magnetar will lose its rotational energy in the form of Poynting-flux, which may be converted into a wind of electron-positron pairs through some magnetic dissipation processes. As proposed by Dai (2004), this wind will catch up with the GRB outflow and a long-lasting reverse shock would form. By applying this scenario to GRB afterglows, we find that the reverse shock propagating back into the electron-positron wind can lead to an observable optical re-brightening and a simultaneous X-ray plateau (or X-ray shallow decay). In our study, we select four GRBs, i.e., GRB 080413B, GRB 090426, GRB 091029, and GRB 100814A, of which the optical afterglows are well observed and show clear re-brightenings. We find that they can be well interpreted. In our scenario, the spin-down timescale of the magnetar should be slightly smaller than the peak time of the re-brightening, which can provide a clue to the characteristics of the magnetar.

Subject headings: gamma-rays: burst — hydrodynamics — radiation mechanisms: non-thermal — methods: numerical

1. INTRODUCTION

Recent multi-wavelength observations of afterglows of gamma-ray bursts (GRBs) have revealed some puzzling features (Panaitescu et al. 2006; Panaitescu & Vestrand 2011; Li et al. 2012; Liang

¹School of Astronomy and Space Science, Nanjing University, Nanjing 210046, China; hyf@nju.edu.cn

²Key Laboratory of Modern Astronomy and Astrophysics (Nanjing University), Ministry of Education, China

³Purple Mountain Observatory, Chinese Academy of Sciences, Nanjing 210008, China; xfwu@pmo.ac.cn

⁴Joint Center for Particle Nuclear Physics and Cosmology of Purple Mountain Observatory-Nanjing University, Chinese Academy of Sciences, Nanjing 210008, China

⁵Department of Physics, Stockholm University, AlbaNova, SE-106 91 Stockholm, Sweden

⁶Erasmus Mundus Joint Doctorate in Relativistic Astrophysics

et al. 2013), impelling the researches on the afterglow theory. X-ray observations from *Swift*/XRT (Gehrels et al. 2004; Burrows et al. 2005) have resulted in diverse light curves, but a canonical light curve consisting of a steep decay, a plateau, and a normal decay phase has been suggested (Zhang et al. 2006). The plateau phase can not be explained in the framework of the simple standard external shock scenario, i.e. synchrotron radiation produced by the interaction of a relativistic ejecta with the circum-burst medium (see Piran et al. 1993; Mészáros & Rees 1997; Sari & Piran 1999 for reviews). On the other hand, some optical afterglows show re-brightenings at late stages ($\sim 10^4 - 10^5$ s), together with a bump occurring in the X-ray band in some cases (e.g., GRB 120326A, Melandri et al. 2014; Hou et al. 2014; Laskar et al. 2015), or without clear counterpart features in X-rays (e.g., GRB 100814A, De Pasquale et al. 2015; GRB 081029, Nardini et al. 2011; GRB 100621A, Greiner et al. 2013). These re-brightenings also deviate from the expectations of the external shock model, which calls for a refined afterglow model.

Several scenarios have been proposed to explain these unexpected features. Some authors invoke energy injection processes (Dai & Lu 1998a,b; Fan & Xu 2006; van Eerten 2014) or forward shocks (FS) refreshed by late shells (Zhang & Mészáros 2002) to produce the X-ray plateau. Meanwhile, circum-burst density enhancements (Dai & Wu 2003; Lazzati et al. 2002), two-component jets (Berger et al. 2003; Huang et al. 2004), or varying microphysical parameters (Kong et al. 2010) have been invoked to explain the optical re-brightenings. However, recent studies indicate the density enhancements model may not work for significant re-brightenings (van Eerten et al. 2009; Gat et al. 2013; Geng et al. 2014). If one wants to interpret a large sample of afterglows, which model is preferred is still uncertain. Although there are various candidate models for afterglows, the possible central engines of GRBs are mainly limited in two kinds of objects. It is generally believed that the central engines of GRBs should either be rapidly spinning, strongly magnetized neutron stars (magnetar, Dai & Lu 1998a,b; Heger et al. 2003; Dai et al. 2006; Metzger et al. 2011; Lü & Zhang 2014) or black holes (Woosley 1993; MacFadyen & Woosley 1999; Lei et al. 2013). This indicates that there is probably a common origin for the optical re-brightenings and the simultaneous X-ray features of a group of afterglows. Therefore, it is reasonable to develop a model which, after taking into account the physics of the central engine, can explain the multi-wavelength afterglows simultaneously.

From the visual perspective, the optical re-brightening seems to be a new component emerging when the flux from the FS gets dim. In the two-component jet model, this kind of late-time component naturally corresponds to a wide jet. However, it may have difficulties in explaining the chromatic evolution of the afterglows in some cases (De Pasquale et al. 2015). The new component can also be generated in another model, i.e., a long-lasting reverse shock (RS) can play the role. If the FS is re-energized by a late outflow (e.g., an electron-positron-pair wind, Dai 2004; Yu & Dai 2007; Yu et al. 2007), then an RS will form behind the FS. As the RS propagating into the outflow, it would contribute to the emission, and its flux can even exceed that from the FS. Moreover, the emission from the RS can help to make diverse light curves in principle since the microphysical parameters may differ from those of the FS. Therefore, it is reasonable to argue that some light

curves with re-brightenings are due to the existence of a long-lasting RS. On the other hand, the long-lasting RS should be common since it is a natural consequence of the energy injection. In previous studies, it has been proposed that continuous energy injections in the form of pure Poynting-flux coming from the central engines may play a key role in explaining some special light curves, through its effects on the evolution of the FS (Zhang et al. 2006; Liu et al. 2009; Geng et al. 2013; Yu et al. 2015). However, in such a scenario without an RS, the emission from the FS could not account for the new components of the re-brightenings discussed here.

In this paper, we propose the ultrarelativistic electron-positron-pair (e^+e^-) wind model to interpret the afterglows with special re-brightenings. After a GRB, the remaining object of the progenitor may be a magnetar, which should lose its rotational energy by ejecting a continuous Poynting-flux. We assume that the Poynting-flux is converted into an ultrarelativistic e^+e^- wind beyond a particular radius ($\sim 10^{15}$ cm). When the e^+e^- wind catches up with the FS, an RS will form and propagate back into the e^+e^- wind. The wind will be shocked and heated by the RS, and radiation from these e^+e^- can account for the optical re-brightenings at late time. It is worthwhile to note that this scenario was originally proposed by Dai (2004) and then used to explain the X-ray plateau and bump by Yu & Dai (2007) and Dai & Liu (2012). However, the method used to solve the shock dynamics in the current work is different and we aim to explain optical re-brightenings. The mechanism of converting the Poynting-flux into ultrarelativistic e^+e^- wind is still unknown. Previous researches indicate that magnetic dissipation may help to explain why pulsar wind nebulae are powered by particle-dominated winds (Rees & Gunn 1974; Lyubarsky & Kirk 2001; Porth et al. 2013; Metzger & Piro 2014). Such a dissipation may also occur in millisecond magnetars.

In our study, we select as examples four GRBs, of which high quality multi-wavelength observational data are available. They are all characterized by optical re-brightenings but without corresponding behaviors being detected in X-rays. We show that they can be well explained in our model. Our paper is organized as follows. In Section 2, we briefly describe the dynamic methods used in our work and the formulae for calculating the radiation. In Section 3, we show how our scenario would work to explain the re-brightenings. The results for each GRB are presented separately in Section 4. The conclusions are summarized in Section 5.

2. HYDRODYNAMICS AND RADIATION

When a relativistic outflow propagates into the circum-burst medium, an FS will form. If the central engine is long-lived and a continuous wind is ejected, an RS is expected to propagate back into the wind. The dynamics of such an FS-RS system can be numerically solved by considering energy conservation as proposed by Geng et al. (2014), or through the mechanical consideration as done by Beloborodov & Uhm (2006; also see Uhm 2011). For clarity, these two methods are described separately in the Appendixes A.1 and A.2.

Now, we show that the dynamical results of these two methods are consistent with each other

within our e^+e^- wind scenario. The Poynting-flux luminosity $L_w(t_{\text{obs}})$ of a newly born magnetar can be derived from the magnetic dipole radiation (Shapiro & Teukolsky 1983), i.e.,

$$L_w \simeq 4.0 \times 10^{47} B_{\text{NS},14}^2 R_{\text{NS},6}^6 P_{\text{NS},-3}^{-4} \left(1 + \frac{t_{\text{obs}}}{T_{\text{sd}}}\right)^{-2} \text{ erg s}^{-1}, \quad (1)$$

where B_{NS} is the strength of the surface magnetic field of the magnetar, R_{NS} is the radius and P_{NS} is its spin period. $T_{\text{sd}} \simeq 5.0 \times 10^4 (1+z) B_{\text{NS},14}^{-2} I_{45} R_{\text{NS},6}^{-6} P_{\text{NS},-3}^2$ s is the spin-down timescale, where I is the moment of inertia of the magnetar. The convention $Q_x = Q/10^x$ in cgs units is adopted hereafter. For simplicity, we fix $I = 10^{45}$ g cm², $R_{\text{NS}} = 10^6$ cm and $P_{\text{NS}} = 1$ ms throughout this work, then L_w is mainly determined by only one parameter, i.e., B_{NS} . We assume the Poynting-flux is converted into an e^+e^- pair wind beyond 10^{15} cm, which is the typical deceleration radius of the outflow. The particle density in the comoving frame of the unshocked wind (or called Region 4) at the radius r is then

$$n'_4 = \frac{L_w}{4\pi r^2 \Gamma_4^2 m_e c^3}, \quad (2)$$

where m_e is the mass of electron, c is the speed of light and Γ_4 is the Lorentz factor of the unshocked wind. Note that the FS-RS system can be divided into four regions (see Appendix A.1), the quantities of Region “ i ” are denoted by subscripts “ i ”. In this paper, the superscript prime (\prime) is used to denote the quantities in the shock comoving frame while characters without prime denote quantities in the observer frame.

For an outflow with an isotropic kinetic energy of $E_{K,\text{iso}} = 1.0 \times 10^{53}$ erg and an initial Lorentz factor of $\Gamma_0 = 300$, we set the number density of the ambient medium n_1 is 1 cm^{-3} , Γ_4 is 10^4 , and B_{NS} is 2×10^{14} G. Then the evolution of the bulk Lorentz factor of the FS (Γ_2) and the RS (Γ_3) can be obtained using the two methods mentioned above. Figure 1 shows the results from the energy conservation method and the mechanical method. We see that the difference between the two solutions is tiny, which means they are consistent with each other. The two solutions approach the solution given by Blandford & McKee (1976) (referred to as the BM solution below) at late times, which is foreseeable since L_w finally becomes very weak and the role of the RS is insignificant. In our following study, we will adopt the mechanical method to solve the dynamics of the FS-RS system.

To calculate the afterglow light curves of the FS-RS system, we consider both the synchrotron radiation and the inverse compton radiation from shock-accelerated electrons. Detailed formulae are described in Appendix B.

3. APPLICATION

In our study, we have collected the afterglow data of four GRBs, i.e., GRB 080413B (Filgas et al. 2011), GRB 090426 (Nicuesa Guelbenzu et al. 2011), GRB 091029 (Filgas et al. 2012) and GRB 100814A (De Pasquale et al. 2015). The observational data are of high quality, and all the

four events show clear optical re-brightenings at $\sim 10^4 - 10^5$ s. The rising of the re-brightenings is generally smooth and shallow, contrary to many other GRBs which brightens sharply (Geng et al. 2013). This indicates the re-brightening component is a result of a continuous behavior, which can be well achieved in our model. A brief summary of the observations of these GRBs is presented in Table 1. We will interpret these afterglows by using our model and discuss the underlying relation between the afterglow behavior and the central engine.

Our sample of afterglows are characterized by a double-bump structure. For the early onset bump (it may not show up due to the lack of early observations), we suggest that it is connected with the typical synchrotron frequency crossing the optical band, or the FS being in the coasting phase. The second re-brightening bump could be due to the emerging RS component at about T_{sd} . We take GRB 100814A as an example to show how this double-bump structure can be consistently reproduced in our model and how the physical parameters can be estimated from analytical derivations. Below, we use the convention $F_{\nu,i} \sim t_{\text{obs}}^{-\alpha} \nu^{-\beta}$, where $F_{\nu,i}$ is the flux density of Region i , α and β are the power-law indices.

The first bump appearing in the optical afterglows of GRB 100814A is roughly at $T_{\text{peak},1} \sim 300$ s and the rising temporal index is $\alpha_{\text{rise}} = -2.5$. In the framework of the external shock model, it indicates that the FS is in the coasting phase (Xue et al. 2009). We assume the isotropic kinetic energy of the outflow is $E_{K,\text{iso}}$, then the initial Lorentz factor Γ_0 can be calculated as $\Gamma_0 = \left[\frac{17E_{K,\text{iso}}(1+z)^3}{64\pi n_1 m_p c^5 T_{\text{peak},1}^3} \right]^{1/8}$. Assuming $E_{K,\text{iso}}$ equals the energy released in the prompt phase ($E_{\gamma,\text{iso}} = 7 \times 10^{52}$ erg) and using typical value of $n_1 = 0.1 \text{ cm}^{-3}$, we obtain $\Gamma_0 \simeq 150$. At the end of the coasting phase, $\nu_{m,2}$ should have crossed the optical band since the observed optical flux decreases after $T_{\text{peak},1}$. This requires $\nu_{m,2}(T_{\text{peak},1}) \leq 10^{15}$ Hz, i.e.,

$$\frac{1}{1+z} \left(\frac{p_2 - 2}{p_2 - 1} \right)^2 \epsilon_{e,2,-1}^2 \epsilon_{B,2,-1}^{1/2} n_{1,0}^{1/2} \leq 3.5 \times 10^{-5}, \quad (3)$$

where z is the redshift of the GRB, p_i is the power-law index of the distribution of electrons in Region i , $\epsilon_{e,i}$ is the fraction of the total energy carried by the electrons, and $\epsilon_{B,i}$ is the ratio of the magnetic field energy to the total energy.

After the coasting phase, we assume the evolution of Γ_2 obeys $\Gamma_2 = AR^{-g}$. According to Section 2, we can still use the BM solution, i.e., $A = \left[\frac{17E_{K,\text{iso}}}{8\pi n_1 m_p c^2} \right]^{1/2}$, and $g = \frac{3}{2}$. Then the typical synchrotron frequency of Region 2 is given by

$$\nu_{m,2} = 5.5 \times 10^{13} \left(\frac{1+z}{2} \right)^{1/2} \left(\frac{p_2 - 2}{p_2 - 1} \right)^2 \epsilon_{e,2,-1}^2 \epsilon_{B,2,-1}^{1/2} E_{K,\text{iso},53}^{1/2} t_{\text{obs,day}}^{-3/2} \text{ Hz}, \quad (4)$$

and the peak flux density at D_L (luminosity distance) is

$$F_{\nu,\text{max},2} = 8.6 \times 10^2 \left(\frac{1+z}{2} \right) \epsilon_{B,2,-1}^{1/2} E_{K,\text{iso},53}^{1/2} n_{1,0}^{1/2} D_{L,28}^{-2} \text{ mJy}. \quad (5)$$

For Region 3, L_w can be taken as a constant within T_{sd} , and the relative Lorentz factor $\Gamma_{43} \simeq \Gamma_4/(2\Gamma_2)$, then the typical synchrotron frequency is given by

$$\nu_{m,3} = 6.9 \times 10^{10} \left(\frac{1+z}{2} \right)^{-3/2} \left(\frac{p_3-2}{p_3-1} \right)^2 L_{w,47}^{1/2} \Gamma_{4,4}^2 \epsilon_{e,3,-1}^2 \epsilon_{B,3,-1}^{1/2} E_{K,iso,53}^{-1/2} n_{1,0}^{1/2} t_{obs,day}^{1/2} \text{ Hz}. \quad (6)$$

The cooling frequency is

$$\nu_{c,3} = 1.4 \times 10^{16} \left(\frac{1+z}{2} \right) L_{w,47}^{-3/2} \epsilon_{B,3,-1}^{-3/2} E_{K,iso,53} n_{1,0}^{-1} t_{obs,day}^{-2} \text{ Hz}, \quad (7)$$

and the peak flux density is

$$F_{\nu,max,3} = 27.4 \left(\frac{1+z}{2} \right)^{1/4} L_{w,47}^{3/2} \Gamma_{4,4}^{-1} \epsilon_{B,3,-1}^{1/2} E_{K,iso,53}^{-1/4} n_{1,0}^{1/4} t_{obs,day}^{3/4} D_{L,28}^{-2} \text{ mJy}. \quad (8)$$

According to Equations (6-7), the condition of $\nu_{m,3} < \nu_{c,3}$ is usually valid within $\sim 10^5$ s.

After the first peak, the optical afterglow enters the slow decay phase, during which the temporal index is $\alpha_{decay} \simeq 0.72$. On the other hand, α_{decay} is predicted as $\frac{3(p_2-1)}{4}$ when $\nu_{m,2} < \nu_{opt} < \nu_{c,2}$, which gives $p_2 \simeq 2.0$.

Just before the emergence of the RS component (i.e., $F_{\nu,3}$), $F_{\nu,2}$ should equal $F_{\nu,3}$ at a certain time. We denote this time as T_{dent} . For the regime $\nu_{m,i} < \nu < \nu_{c,i}$, we have $F_{\nu,i} = F_{\nu,max,i} \left(\frac{\nu}{\nu_{m,i}} \right)^{-(p_i-1)/2}$. The g band data shows $T_{dent} \simeq 1.2 \times 10^4$ s, and the flux density at T_{dent} is $\simeq 7 \times 10^{-2}$ mJy. Therefore we can get $F_{\nu,2}(T_{dent}) = F_{\nu,3}(T_{dent}) = 3.5 \times 10^{-2}$ mJy, which further gives

$$\begin{aligned} & \left(\frac{1+z}{2} \right)^{(p_2+3)/4} \left(\frac{p_2-2}{p_2-1} \right)^{p_2-1} \epsilon_{e,2,-1}^{p_2-1} \epsilon_{B,2,-1}^{(p_2+1)/4} E_{K,iso,53}^{-(p_2+3)/4} n_{1,0}^{1/2} D_{L,28}^{-2} \\ & = 4.1 \times 10^{-5} \left(\frac{\nu_{opt}}{1.1 \times 10^{15} \text{ Hz}} \right)^{(p_2-1)/2}, \end{aligned} \quad (9)$$

and

$$\begin{aligned} & \left(\frac{1+z}{2} \right)^{(-3p_3+4)/4} \left(\frac{p_3-2}{p_3-1} \right)^{p_3-1} \epsilon_{e,3,-1}^{p_3-1} \epsilon_{B,3,-1}^{(p_3+1)/4} E_{K,iso,53}^{-p_3/4} n_{1,0}^{p_3/4} L_{w,47}^{(p_3+5)/4} \Gamma_{4,4}^{p_3-2} D_{L,28}^{-2} \\ & = 5.6 \times 10^{-3} \left(\frac{\nu_{opt}}{2.6 \times 10^{10} \text{ Hz}} \right)^{(p_3-1)/2}, \end{aligned} \quad (10)$$

where $\nu_{opt} = 6.4 \times 10^{14}$ Hz.

The flux from the RS should reach its peak at T_{sd} since the flux decays when $t_{obs} > T_{sd}$ (see below). In principle we can set T_{sd} as the peak time of the second bump, e.g, $T_{sd} = T_{peak,2}$. However, the effect of the equal arrival time surface (EATS) would delay the peak time in the optical bands. On the other side, the peak time in X-rays will be less affected. In the case of GRB

100814A, we notice that there may be a small structure in the X-ray afterglow at $\sim 4 \times 10^4$ s, which gives $T_{\text{sd}} \simeq 4 \times 10^4$ s. We take $I = 10^{45}$ g cm², $R_{\text{NS}} = 10^6$ cm and $P_{\text{NS}} = 1$ ms as typical values, then B_{NS} can be constrained from T_{sd} , and L_{w} can be obtained from Equation (1).

When $T_{\text{dent}} < t_{\text{obs}} < T_{\text{peak},2}$, L_{w} cannot be treated as constant since t_{obs} is approaching T_{sd} . In this case, we have $\nu_{m,3} \propto L_{\text{w}}^{1/2} t_{\text{obs}}^{1/2}$, $F_{\nu,\text{max},3} \propto L_{\text{w}}^{3/2} t_{\text{obs}}^{3/4}$, and $F_{\nu,3} \propto \nu_{m,3}^{(p_3-1)/2} F_{\nu,\text{max},3} \propto L_{\text{w}}^{(p_3+5)/4} t_{\text{obs}}^{(p_3+2)/4}$. A power-law fitting to this segment gives the observed temporal index as $\simeq -0.5$. If we assume the evolution of L_{w} during this segment is roughly $\propto t_{\text{obs}}^{-0.3}$, then p_3 can be inferred to be 2.4. After the second peak ($t_{\text{obs}} > T_{\text{peak},2}$), since L_{w} evolves as $\propto t_{\text{obs}}^{-2}$, $\nu_{m,3}$ will decay with time and $\nu_{c,3}$ will increase. As a result, none of them will cross the optical band, i.e. $\nu_{m,3} < \nu_{\text{opt}} < \nu_{c,3}$. The optical spectral index at this time becomes ~ 0.7 , which further gives $p_3 = 2.4$ since $(p_3-1)/2 = 0.7$. This value is consistent with that obtained before.

The jet break time t_j is hard to determine since the FS flux is always lower than that of the RS component after T_{dent} . In our fitting, we assume $t_j \simeq 10^5$ s, which requires the half-opening angle of the jet $\theta_j \sim 0.058$ rad (Lu et al. 2012). We have little knowledge on the bulk Lorentz factor of the e^+e^- wind, Γ_4 . However, a value ranging from 10^4 to 10^6 may be reasonable (Yu et al. 2007). For GRB 100814A, we take $\Gamma_4 \simeq 10^5$. There are still four free parameters left, i.e., $\epsilon_{e,2}$, $\epsilon_{B,2}$, $\epsilon_{e,3}$ and $\epsilon_{B,3}$. Using conditions given in Equations (3), (9-10), and an underlying relation $\epsilon_{e,3} = 1 - \epsilon_{B,3}$, we get $\epsilon_{e,2} \simeq 5.5 \times 10^{-2}$, $\epsilon_{B,2} \simeq 1.2 \times 10^{-3}$, and $\epsilon_{B,3} \simeq 0.02$. In our subsequent study, we use these parameter values as a guide to perform numerical calculations, adjusting the parameters slightly to get a visually good agreement to the observed afterglow light curves (see Figure 2). The final values (see in Table 2) of the parameters do not deviate significantly from the above derivations. The high-energy γ -ray afterglow of GRB 100814A is also calculated. Figure 3 presents the flux density at 100 MeV, in which the SSC flux from the RS leads to a small bump in the light curve at $\sim 10^5$ s. This is a special feature predicted by our model. High-energy observations in the future can help to test the prediction. We apply the above procedure to the afterglows of other three GRBs (see Figures 4-6). The derived parameters are also listed in Table 2.

In order to provide a meaningful constraint on the parameters, we make use of the data fitting code named emcee (Foreman-Mackey et al. 2013), which is a widely used tool based on the Markov chain Monte Carlo (MCMC) simulations. There are totally 11 parameters for each GRB. It would be difficult to solve the problem if we set all these parameters as free parameters. The degeneracy between the parameters is one major reason. Even for 7 parameters related to the FS, this degeneracy may be significant (Ryan et al. 2013; van Eerten 2015). The other reason is the incredible computational cost in the MCMC sampling. Since we are mostly interested in the parameters connected with the RS, we finally chose B_{NS} , Γ_4 and $\epsilon_{B,3}$ as free parameters. The allowed ranges of these parameters in the Monte Carlo simulation is set to be $[0.1,100] \times 10^{14}$ G, $[0.1,100]$ and $[1.0 \times 10^{-6}, 0.9]$ respectively. Other parameters are fixed by using the values of Table 2. The simulation results are presented in Table 3. Figure 7 shows the corner plot of the fit for GRB 080413B as an example, which consists of the marginalized distributions of each parameter and the covariances between pairs of parameters.

The sensitivity of the results (in Table 3) on fixing other parameters can be roughly analysed. In order to approach a good fitting to a specific light curve with re-brightening, the early afterglow is attributed to the FS and the re-brightening is attributed to the RS. In the case of small B_{NS} (the re-brightening occurs relatively late), the dynamics of the FS is slightly affected by the e^+e^- wind. That would make some FS parameters independent of the RS parameters. Taking GRB 080413B as an example, the early peak of the afterglow indicates $\nu_{m,2}$ should be crossing the optical band at $\sim 10^2$ s (Figure 4). If one applies the MCMC fitting with the FS parameters, according to Equations (4) and (5), one would find $\epsilon_{B,2}$ and $E_{K,\text{iso}}$ are degenerate in some extent, and they are in negative correlation with $\epsilon_{e,2}$ or n_1 (also see Figure 1 in Ryan et al. 2013). On the other hand, according to Equation (10), $E_{K,\text{iso}}$ and n_1 would be involved in calculations of the flux from the RS. Both of them are expected to be negatively correlated with Γ_4 in the corner plot. To judge whether the results in Table 3 are meaningful, we can do the following experiment. Now, we fix the parameters in Table 3, and leave parameters $\epsilon_{e,2}$, $\epsilon_{B,2}$, n_1 free. The MCMC fitting (see Figure 8) gives $\epsilon_{e,2} = 0.043_{-0.009}^{+0.013}$, $\epsilon_{B,2} = 0.027_{-0.008}^{+0.011}$, $n_1 = 0.12_{-0.006}^{+0.005}$ respectively. These values do not deviate much from those in Table 2. In Figure 8, we can see n_1 is well constrained, which implies the results in Table 3 are sensitive to n_1 . This could be understandable since n_1 is involved in the calculation of the dynamics of the RS and other parameters of the RS are fixed now. This feature implies that the results in Table 3 would become robust when the early observational data (mainly related with the FS) could constrain parameters $E_{K,\text{iso}}$ and n_1 well.

4. DISCUSSIONS

The four GRBs studied here actually have been investigated by other authors in the literature. Previous efforts failed to explain many of the puzzling behaviors of these events. Here, we would like to discuss how our mechanism can improve the modeling.

4.1. GRB 080413B

The afterglow of GRB 080413B has been explained by the on-axis two-component jet model (Filgas et al. 2011). In this model, the narrow ultra-relativistic jet is responsible for the initial decay, while the moderately relativistic wide jet is expected to account for the late re-brightening. The collapsar model of long-duration GRBs offers a possible mechanism for generating a two-component jet (Ramirez-Ruiz et al. 2002; Kumar & Zhang 2015). According to Filgas et al. (2011), the power-law index of the narrow jet electrons can be derived as $p \simeq 1.44$ ($\nu_m < \nu_{\text{opt}} < \nu_c$) from the observed optical temporal index of $\alpha \simeq 0.73$. However, such an electron distribution with p significantly less than 2 seems to be too hard. Simulation on Fermi acceleration of charged particles by relativistic shocks indicates p is $\simeq 2.26 \pm 0.04$ in the ultrarelativistic limit $\Gamma \gg 1$ (Lemoine & Pelletier 2003). The investigation on the distribution of p from *Swift* GRB afterglows supports a Gaussian distribution centered at $p = 2.36$ with a width of 0.59 (Curran et al. 2010).

In our model, this difficulty no longer exists. The evolution of the Lorentz factor of FS before T_{sd} deviates from the BM solution ($\Gamma \propto R^{-g}$, $g = \frac{3}{2}$) due to the effect of the e^+e^- wind, i.e., g should be $< \frac{3}{2}$. Using the closure relation of $0.73 = \frac{4g}{2g+1} \frac{p_2-1}{2}$, we can obtain $p_2 = 2.1$ if $g \simeq 1$. Thus we can fit the light curves with a reasonable p . Additionally, in the two-component jet model, the optical spectral index (pre-jet break) of $\alpha \simeq 0.9$ indicates $p = 1.8$ ($\nu_{\text{opt}} > \nu_c > \nu_m$) for the wide jet. In our model, ν_c is greater than ν_{opt} but slightly smaller than ν_X , which gives $p_3 = 2.8$ (see in Table 2). This value again is more acceptable.

4.2. GRB 090426

GRB 090426 is a short GRB according to its duration (Nicuesa Guelbenzu et al. 2011). However, some authors argued that GRB 090426 may be connected with a collapsar event, rather than the merger of two compact objects (Antonelli et al. 2009; Xin et al. 2011; Levesque et al. 2010). In this case, a magnetar could be naturally involved. The high density of $n_1 = 50 \text{ cm}^{-3}$ derived from our fitting is consistent with the lower limit of 10 cm^{-3} given by Xin et al. (2011). The optical and X-ray light curves of GRB 090426 could be fitted by the two-component jet model of Nicuesa Guelbenzu et al. (2011). But we notice that the first break (around 300 s) in the R_c band light curve cannot be explained by the jet break of the narrow-jet component (Nicuesa Guelbenzu et al. 2011). On the contrary, it can be reasonably explained as the cessation of the energy injection episode (Xin et al. 2011). This is a natural consequence of our model. We have shown that the dynamics of the FS is significantly affected by the e^+e^- wind at early times, but it should be in accord with the BM solution at late stages. In Figure 5, we can see that this break corresponds to the turn over of the evolution of $\nu_{c,\text{FS}}$. According to Nicuesa Guelbenzu et al. (2011), the steep decay of the optical afterglow after 3×10^4 s is due to the sideways expansion of the wide jet. However, the sideways expansion of a relativistic jet may be a very slow process (Zhang & MacFadyen 2009), which disfavors the short interval between the peak time ($\sim 10^4$ s) and the jet break time in GRB 090426. In our scenario, this steep decay is a natural result of the quick decline of L_w after the spin-down timescale.

4.3. GRB 091029

The optical and X-ray light curves of the afterglow of GRB 091029 are not similar to each other and are hard to be explained by a simple model. It is very peculiar that the optical spectral index decreases between 0.4 ks and 9 ks, and increases later, but at the same time, the X-ray spectral index is almost a constant. Filgas et al. (2012) examined several scenarios and argued that a two-component jet can basically explain the observations. The hardening of the optical spectrum can be explained by assuming that the electron power-law index changes with time. In our scenario, the hardening of the optical spectrum before 10^4 s is also due to the varying electron index p of the FS (Filgas et al. 2012; Kong et al. 2010). But after 10^4 s, the softening of the optical spectrum is

caused by the rising flux from the RS. According to Filgas et al. (2012), the X-ray spectral index is $\simeq 1.1$ over the entire time window. In our model, the X-ray band is in the $\nu > \nu_c > \nu_m$ regime at 10^3 s, which leads to $p_2 = 2.2$. Note that the optical flux from the RS should be dominated after 10^4 s, p_3 should be relatively larger in order to match the softening spectrum. In our numerical calculations, we finally takes $p_2 = 2.2$, $p_3 = 2.3$. The broad-band afterglow of GRB 091029 can be fitted quite well.

4.4. GRB 100814A

Possible interpretations for the afterglow of GRB 100814A have been discussed by De Pasquale et al. (2015). In De Pasquale et al. (2015), the optical re-brightenings are attributed to the FS, when ν_m of the FS is crossing the optical band, and the RS is generated by the late shells that collide with the trailing ones. In our scenario, the re-brightening is due to the emerging of the RS flux, while the RS forms due to the injection of continuous e^+e^- winds. Our numerical results indicate that the optical flux from the FS peaks at around 400 s, when ν_m of the FS crosses the optical band (see the lower panel of Figure 2). The observed R_c band light curve (see Figure 2 of De Pasquale et al. 2015) does show an early peak, which is consistent with our results.

5. CONCLUSIONS

Optical re-brightenings appearing at $\sim 10^4$ s in the afterglows of some GRBs may come from a common origin. In this work, we attribute the re-brightenings to the RS propagating into the ultrarelativistic e^+e^- wind ejected by the central engine. We compared two methods used for solving the dynamics and found that they are both appropriate in describing the FS-RS system. Multi-wavelength afterglows of four GRBs can be well explained in the framework of our scenario.

The success of our model can give helpful information on the central engine of these GRBs. T_{sd} can be derived from the X-ray peak time of the RS component as described in Section 3, which could give clues on the characteristics of the newly born magnetar. Generally, an earlier re-brightening means B_{NS} is larger or P_{NS} is smaller, i.e., the magnetar losses its energy more quickly. In the future, if the observational data can help to constrain the parameters of the FS well enough, we will be able to derive B_{NS} more accurately by using the re-brightening. It will be a useful way to probe the characteristics of the magnetar. Note that the derived values of Γ_4 of GRB 091029 and GRB 100814A are larger than those of the other two GRBs. It means that the efficiency of converting the Poynting-flux to the kinetic energy of particles is higher in these cases.

Observationally, it seems there are no equivalent features in X-rays around the optical re-brightenings. However, the predicted emission near $T_{peak,2}$ in both optical and X-ray wavelengths is dominated by the RS component in our model. There are two main factors to result in this puzzle. First, the actual peak time of the RS component in optical bands is delayed ($> T_{sd}$) by

the EATS effect, which causes the flux ratio $F_{\text{opt},3}/F_{\text{opt},2}$ to be relatively larger since $F_{\text{opt},2}$ is decreasing. Second, at the X-ray peak time, the flux ratio of $F_{X,3}/F_{X,2}$ is expected to be relatively small. Moreover, the emerging of the RS component in X-rays is essential to produce the X-ray plateau, otherwise the X-ray light curve will decay as a power-law after $T_{\text{peak},1}$ (see $F_{\nu,2}$ in Figure 2). In other words, the X-ray plateau should be a common feature accompanying the optical re-brightening.

The fact that the re-brightening time is coincident with T_{sd} , together with the arguments that magnetars could serve as the central engines of GRBs in recent years, motivates us to suggest that there may be a common origin for the re-brightening. e^+e^- winds are natural outcome from magnetars, as hinted from phenomena associated with pulsar wind nebulae. Thus we believe our scenario could work well and it is physically reasonable. Of course, the models involving late shells with a range of velocities may also produce the similar results. Further study on the form of the injected energy are thus called to give a conclusion. In principle, the mass density is different between a baryonic shell and an electron-positron wind. But it is not clear how the mass density can be measured from observations. For the baryonic shell, one may calculate the total mass of the shell to check whether it is reasonable.

In the future, two potential ways should help to discriminate between our e^+e^- winds model and models involving baryons-dominated shells. First, the high energy emission (> 100 MeV) should be more significant when the continuously injected energy is carried by leptons rather than baryons, since IC scattering will be much stronger (Yu et al. 2007). As an example, Fig. 3 shows that the SSC flux from the RS exceeds the synchrotron emission from the FS at late times in the case of GRB 100814A. If a high energy bump is observed near the peak time of the optical re-brightening, it will be a strong evidence for the e^+e^- wind. Furthermore, the evolution of the polarization degree during the plateau or the re-brightening phase in two models are significantly different (Lan et al. 2016). Therefore, the observations on the high energy emission and the polarization during the re-brightening phase would identify which model is preferred.

The e^+e^- wind scenario is not necessarily based on magnetars as central engines. A newly born BH accompanied by an accretion disk may also emit continuous Poynting-flux (Blandford & Znajek 1977) and the luminosity evolution may somehow be similar to that of a magnetar (Equation 1). Such a BH can also serve as the central engine in our model. In our model, the Poynting-flux is assumed to be converted to an e^+e^- wind efficiently, but note that the possibility of this conversion and its efficiency are still quite uncertain for a newly born magnetar. A more general treatment is to introduce a magnetization parameter σ to describe the late ejecta (Zhang & Kobayashi 2005), and this may affect the RS emission if σ is significantly larger than 1. The diversity of σ would also help to explain why optical re-brightenings do not appear in some GRB afterglows. For a magnetized ejecta, the parameters derived may be correspondingly different. However, the main conclusions of this study would remain unchanged.

We are very grateful to an anonymous referee for valuable suggestions. We thank Yiming Hu

and Bing Zhang for helpful discussions. This work was supported by the National Basic Research Program (“973” Program) of China (grant Nos. 2014CB845800 and 2013CB834900) and the National Natural Science Foundation of China (grant Nos. 11473012, 11573014 and 11322328). X. F. Wu acknowledges support by the One-Hundred-Talents Program, the Youth Innovation Promotion Association (2011231), and the Strategic Priority Research Program “The Emergence of Cosmological Structures” of the Chinese Academy of Sciences (Grant No. XDB09000000). Liang Li acknowledges support by the Swedish National Space Board, and the Erasmus Mundus Joint Doctorate Program by Grant Number 2013-1471 from the EACEA of the European Commission. This work made use of data supplied by the UK Swift Science Data Center at the University of Leicester.

A. HYDRODYNAMICS

A.1. Energy Conservation Method

Let’s consider a relativistic outflow with an initial mass of M_{ej} propagating into a cold interstellar medium (ISM). Two shocks separate the system into four regions: (1) the unshocked ISM, (2) the shocked ISM, (3) the shocked wind, and (4) the unshocked wind. Regions 2 and 3 can be regarded as simple homogenous shells (Piran 1999). In this paper, the quantities (e.g., the electron Lorentz factor γ_e , internal energy U , and pressure p) of Region “ i ” are denoted by subscripts “ i ”, and the superscript prime (\prime) is used to denote the quantities in the shock comoving frame while characters without prime denote quantities in the observer frame.

The FS and the RS can be described by a common bulk Lorentz factor $\Gamma_2 = \Gamma_3 = \Gamma$ (the corresponding dimensionless speed is β) and we assume the Lorentz factor of the unshocked wind is Γ_4 . Below, Γ_{ij} and β_{ij} are the relative Lorentz factor and dimensionless speed of Region “ i ” as measured in the frame of Region “ j ”. Applying the jump conditions to the FS, the thermodynamical quantities of the gases in the rest frame of Region 2 are given by: $U'_2 = (\Gamma - 1)m_2c^2$ (internal energy) and $p'_2V'_2 = (\hat{\gamma}_2 - 1)U'_2$ (product of pressure and volume), where m_2 is the total mass swept by the FS, $\hat{\gamma}_2 \simeq (4\Gamma + 1)/(3\Gamma)$ is the adiabatic index and c is the speed of light. If the fraction of the thermal energy lost due to radiation is ϵ_2 (i.e., the radiation efficiency), then the energy of Region 2 is (Pe’er 2012; Geng et al. 2014)

$$H_2 \simeq (\Gamma - 1)(m_2 + M_{\text{ej}})c^2 + (1 - \epsilon_2)\Gamma(U'_2 + p'_2V'_2). \quad (\text{A1})$$

Taking ϵ_e as the equipartition parameter for shocked electrons, the radiation efficiency can be calculated as $\epsilon_2 = \epsilon_e t'_{\text{syn}}^{-1}/(t'_{\text{syn}}^{-1} + t'_{\text{ex}}^{-1})$ (Dai & Lu 1999), where t'_{syn} is the synchrotron cooling timescale and $t'_{\text{ex}} = R/(\Gamma c)$ is the expansion timescale in the comoving frame. Similarly, the energy of Region 3 is

$$H_3 \simeq (\Gamma - 1)m_3c^2 + (1 - \epsilon_3)\Gamma(U'_3 + p'_3V'_3), \quad (\text{A2})$$

where $U'_3 = (\Gamma_{43} - 1)m_3c^2$ and $p'_3V'_3 = (\hat{\gamma}_3 - 1)U'_3$. The adiabatic index of Region 3 can be

approximated as $\hat{\gamma}_3 \simeq (4\Gamma_{43} + 1)/3\Gamma_{43}$. The total energy of the matter between the FS and the RS is thus $H_{\text{tot}} = H_2 + H_3$.

We can derive the differential equation for the evolution of Γ following the procedure of Huang et al. (1999, 2000) and Geng et al. (2014). When a mass of dm_2 of the ISM is swept up by the FS, a fraction of thermal energy, $dE_{\text{loss}} = \epsilon_2 \Gamma \hat{\gamma}_2 (\Gamma - 1) dm_2 c^2$ would be radiated from Region 2. Similarly, when the wind matter of mass dm_3 is swept up by the RS, Region 3 will gain some thermal energy, i.e., $dE_{\text{gain}} = (1 - \epsilon_3) \Gamma \hat{\gamma}_3 (\Gamma_{43} - 1) dm_3 c^2$. Using $dH_{\text{tot}} = dE_{\text{gain}} - dE_{\text{loss}}$, $d\Gamma_{43}/d\Gamma = -\beta_{43} \Gamma_{43}/\beta \Gamma$ ($\Gamma_4 = \text{constant}$), and the relevant formulae above, we have

$$\frac{d\Gamma}{dm_2} = \frac{f_2}{f_1} + \frac{f_3}{f_1} \frac{dm_3}{dm_2}, \quad (\text{A3})$$

where $f_1 = M_{\text{ej}} + m_2 + m_3 + \frac{1}{3}(1 - \epsilon_2)(8\Gamma - 3)m_2 + \frac{1}{3}(1 - \epsilon_3)[4\Gamma_{43} - 3 - \frac{1}{\Gamma_{43}} - \frac{\beta_{43}}{\beta}(4\Gamma_{43} + \frac{1}{\Gamma_{43}})]m_3$, $f_2 = -\frac{4}{3}(\Gamma^2 - 1)$, and $f_3 = -(\Gamma - 1)$. On the other hand, it can be derived that (see Geng et al. 2014)

$$\frac{dm_3}{dm_2} = \left(\frac{\beta_4}{\beta} - 1 \right) \frac{\rho'_4}{\rho_1} \Gamma_4, \quad (\text{A4})$$

where ρ'_4 is the comoving density of Region 4 and ρ_1 is the density of the circum-burst environment. The evolution of Γ can thus be calculated by using Equation (A3).

A.2. Mechanical Method

Another method to solve the dynamics of the FS-RS system is developed by Beloborodov & Uhm (2006). Here, we briefly describe this mechanical method. In this method, the shocked Regions 2 and 3 between the FS and RS are called the “blast” and the blast is assumed to move with a Lorentz factor Γ (the corresponding dimensionless speed is β). In this section, the subscription “ f ” or “ r ” is used to denote the quantities just behind the FS or the RS, thus the velocities (relative to the shock front) of the postshock medium are β_f and β_r respectively. Considering the conservation of energy-momentum and mass flux in Regions 2 and 3 between the FS (r_f) and the RS (r_r), three equations can be obtained

$$\frac{1}{r^2 c} \frac{d}{dt} (r^2 \Sigma \Gamma) - \Gamma [\rho_r (\beta - \beta_r) + \rho_f (\beta_f - \beta)] = 0, \quad (\text{A5})$$

$$\frac{1}{r^2 c} \frac{d}{dt} (r^2 H \Gamma^2 \beta) - \Gamma^2 \beta [h_r (\beta - \beta_r) + h_f (\beta_f - \beta)] = p_r - p_f, \quad (\text{A6})$$

$$\frac{1}{r^2 c} \frac{d}{dt} (r^2 H \Gamma) - \Gamma [h_r (\beta - \beta_r) + \rho_f (\beta_f - \beta)] = \frac{\Gamma}{c} \frac{d}{dt} P - \Gamma [p_r (\beta - \beta_r) + p_f (\beta_f - \beta)], \quad (\text{A7})$$

where $\Sigma = \int_{r_r}^{r_f} \rho dr$, $H = \int_{r_r}^{r_f} h dr$, $P = \int_{r_r}^{r_f} p dr$, and $H - \Sigma c^2 = 4P$, ρ , h , p are the mass density, energy density and pressure measured in the rest frame of the FS, respectively. Other equations derived from shock jump conditions are needed to complete the equations above (see Uhm 2011; Uhm et al. 2012 for details). These equations can be solved numerically, and Γ can be obtained together with Σ , H , and P .

B. RADIATION

Electrons will be accelerated by the FS and the RS after the shocks. As usual, we assume the accelerated electrons carry a fraction $\epsilon_{e,i}$ of the total energy and the ratio of the magnetic field energy to the total energy is $\epsilon_{B,i}$. In the absence of radiation loss, the energy distribution of the shocked electrons is usually assumed to be a power-law as $dN'_{e,i}/d\gamma'_{e,i} \propto \gamma'^{-p_i} (\gamma'_{m,i} \leq \gamma'_{e,i} \leq \gamma'_{M,i})$, where $\gamma'_{e,i}$ is the Lorentz factor of electrons of Region i , and p_i is the spectral index.

The minimum Lorentz factor is

$$\gamma'_{m,i} = \zeta_i \epsilon_{e,i} \frac{p-2}{p-1} (\hat{\Gamma}_i - 1) + 1, \quad (\text{B1})$$

where $\zeta_2 = m_p/m_e$ (m_p and m_e are the mass of protons and electrons respectively), $\zeta_3 = 1$, $\hat{\Gamma}_2 = \Gamma_2$, and $\hat{\Gamma}_3 = \Gamma_{43}$. The maximum Lorentz factor is

$$\gamma'_{M,i} \simeq 10^8 [B'_i(1 + Y_i)]^{-1/2}, \quad (\text{B2})$$

where B'_i is the comoving magnetic field strength, and Y_i is the Compton parameter that is defined as the ratio of the inverse compton (IC) power to the synchrotron power. The Compton parameter of an electron with Lorentz factor of γ'_e can be determined by $Y_i(\gamma'_e) = (-1 + \sqrt{1 + 4\eta_{\text{rad},i}\eta_{\text{KN},i}\epsilon_{e,i}/\epsilon_{B,i}})/2$ (Fan & Piran 2006; He et al. 2009), where $\eta_{\text{rad},i}$ is the fraction of energy that is radiated due to synchrotron and IC radiation, $\eta_{\text{KN},i}$ is the fraction of synchrotron photons with energy below the Klein-Nishina limit.

Considering the radiation loss, the actual electron distribution would be characterized by the cooling Lorentz factor $\gamma'_{c,i}$, which is given by

$$\gamma'_{c,i} = \frac{6\pi m_e c(1+z)}{(1+Y_i)\sigma_T B_i'^2 (\Gamma_i + \sqrt{\Gamma_i^2 - 1}) t_{\text{obs}}}, \quad (\text{B3})$$

where t_{obs} is the time measured in the observer's frame and σ_T is the Thomson cross section. Then, the actual electron distribution should be given as the following cases: 1. for $\gamma'_{c,i} \leq \gamma'_{m,i}$,

$$\frac{dN'_{e,i}}{d\gamma'_{e,i}} \propto \begin{cases} \gamma'^{-2}_{e,i}, & \gamma'_{c,i} \leq \gamma'_{e,i} \leq \gamma'_{m,i}, \\ \gamma'^{-p_i-1}_{e,i}, & \gamma'_{m,i} < \gamma'_{e,i} \leq \gamma'_{M,i}. \end{cases} \quad (\text{B4})$$

2. for $\gamma'_{m,i} < \gamma'_{c,i} \leq \gamma'_{M,i}$,

$$\frac{dN'_{e,i}}{d\gamma'_{e,i}} \propto \begin{cases} \gamma'^{-p_i}_{e,i}, & \gamma'_{m,i} \leq \gamma'_{e,i} \leq \gamma'_{c,i}, \\ \gamma'^{-p_i-1}_{e,i}, & \gamma'_{c,i} < \gamma'_{e,i} \leq \gamma'_{M,i}. \end{cases} \quad (\text{B5})$$

With the electron distribution determined, the synchrotron emissivity of electrons in Region i at frequency ν' can be calculated as (Rybicki & Lightman 1979)

$$\varepsilon'_{i,\text{syn}}(\nu') = \frac{\sqrt{3}q_e^3 B'_i}{m_e c^2} \int_{\min\{\gamma'_{m,i}, \gamma'_{c,i}\}}^{\gamma'_{M,i}} \frac{dN'_{e,i}}{d\gamma'_{e,i}} F\left(\frac{\nu'}{\nu'_{\text{ch}}}\right) d\gamma'_{e,i}, \quad (\text{B6})$$

where $\nu'_{\text{ch}} = 3\gamma'_{e,i}{}^2 q_e B'_i / (4\pi m_e c)$, q_e is the electric charge of an electron, $F(x) = x \int_x^\infty K_{5/3}(x) dx$, with $K_{5/3}(x)$ being the Bessel function. The synchrotron self-absorption (SSA) effect should be taken into account (Rybicki & Lightman 1979; Wu et al. 2003). In our calculation, the absorption effect can be included by multiplying a factor to the emissivity above. For the shell geometry, the absorption factor is expressed as $(1 - e^{-\tau_{\nu'}}) / \tau_{\nu'}$, where $\tau_{\nu'}$ is the optical depth. The self-absorption coefficients $\kappa_{\nu'}$ can be derived analytically (see Appendix C), which further gives $\tau_{\nu'} = \kappa_{\nu'} \Delta = \frac{\kappa_{\nu'}}{n_e} \frac{N_{e,\text{tot}}}{\Omega R^2}$, where $N_{e,\text{tot}}$ is the total number of electrons, Δ is the width of the shell, $\Omega = 2\pi(1 - \cos \theta_j)$ is the solid angle of the outflow, and θ_j is the half-opening angle of the jet.

Besides the synchrotron radiation, electrons would be cooled by IC scattering of seed photons. IC scattering by self-emitted synchrotron photons is referred as synchrotron self-Compton (SSC) process, and IC scattering by photons from other regions is referred to as cross inverse-Compton (CIC) process. If the flux density of seed photons of Region j is $f_{\nu',s,j}$, the IC ($i = j$ for SSC and $i \neq j$ for CIC) emissivity at frequency ν' is calculated by (Blumenthal & Gould 1970; Yu et al. 2007)

$$\varepsilon'_{i,\text{IC}}(\nu') = 3\sigma_{\text{T}} \int_{\gamma'_{\text{min},i}}^{\gamma'_{\text{M},i}} \frac{dN'_{e,i}}{d\gamma'_{e,i}} d\gamma'_{e,i} \int_{\nu'_{s,j,\text{min}}}^{\infty} d\nu'_{s,j} \frac{\nu' f'_{\nu',s,j}}{4\gamma'_{e,i}{}^2 \nu'^2_{s,j}} g(x, y), \quad (\text{B7})$$

where $\gamma'_{\text{min},i} = \max[\min[\gamma'_{c,i}, \gamma'_{m,i}], h\nu' / (m_e c^2)]$, $\nu'_{s,j,\text{min}} = \nu' m_e c^2 / [4\gamma'_{e,i}(\gamma'_{e,i} m_e c^2 - h\nu')]$, $x = 4\gamma'_{e,i} h\nu'_{s,j} / m_e c^2$, $y = h\nu' / [x(\gamma'_{e,i} m_e c^2 - h\nu')]$, and $g(x, y) = 2y \ln y + (1 + 2y)(1 - y) + \frac{x^2 y^2}{2(1+xy)}(1 - y)$.

Let θ be the angle between the velocity of the emitting material and the line of sight, the Doppler factor is then $\mathcal{D}_i = 1/[\Gamma_i(1 - \beta_i \cos \theta)]$. The observed synchrotron and IC flux densities at frequency ν ($\nu = \nu' / \mathcal{D}_i$) from Region i are given by

$$F_{\nu,i}^{\text{syn}} = \int_0^{\theta_j} d\theta V'_i(\theta) \frac{\sin \theta}{1 - \cos \theta_j} \frac{\mathcal{D}_i^3 \varepsilon'_{i,\text{syn}}(\mathcal{D}_i^{-1} \nu)}{4\pi D_L^2}, \quad (\text{B8})$$

$$F_{\nu,i}^{\text{IC}} = \int_0^{\theta_j} d\theta V'_i(\theta) \frac{\sin \theta}{1 - \cos \theta_j} \frac{\mathcal{D}_i^3 \varepsilon'_{i,\text{IC}}(\mathcal{D}_i^{-1} \nu)}{4\pi D_L^2}, \quad (\text{B9})$$

where $V'_i(\theta)$ is the volume of the emitting material. The luminosity distance D_L is obtained by adopting a flat Λ CDM universe, in which $H_0 = 71 \text{ km s}^{-1}$, $\Omega_{\text{m}} = 0.27$, and $\Omega_{\Lambda} = 0.73$. In our calculations, the integration is performed over the equal-arrival-time surface (EATS, Waxman 1997; Granot et al. 1999; Huang et al. 2007). The EATS (or a sequence of V'_i) at t_{obs} is determined by

$$t_{\text{obs}} = (1 + z) \int_0^{R_\theta} \frac{1 - \beta_i \cos \theta}{\beta_i c} dr \equiv \text{const}, \quad (\text{B10})$$

from which R_θ (or $V'_i(\theta)$) can be derived for a given θ .

C. SYNCHROTRON SELF-ABSORPTION COEFFICIENTS

In this section, as an example, we consider only one emitting region, thus we remove the subscript i . In the comoving frame, the synchrotron radiation power at frequency ν' from an

electron of γ'_e is

$$P'(\nu') = \frac{\sqrt{3}q_e^3 B'}{m_e c^2} F\left(\frac{\nu'}{\nu'_{\text{ch}}}\right) = C_0 F\left(\frac{\nu'}{\nu'_{\text{ch}}}\right), \quad (\text{C1})$$

where $\nu'_{\text{ch}} = 3\gamma_e'^2 q_e B' / (4\pi m_e c)$. For electrons with a distribution of $dN'_e/d\gamma'_e$, the self-absorption coefficient at frequency ν' can be calculated as (Rybicki & Lightman 1979)

$$\kappa_{\nu'} = -\frac{1}{8\pi m_e \nu'^2} \int_{\min[\gamma'_{e,m}, \gamma'_{e,c}]^{\gamma'_{e,M}}} \gamma_e'^2 \frac{d}{d\gamma'_e} \left[\frac{1}{\gamma_e'^2} \frac{dN'_e}{d\gamma'_e} \right] P'(\nu', \gamma'_e) d\gamma'_e. \quad (\text{C2})$$

Define $x = \nu' / \nu'_{\text{ch}}$, then $\gamma'_e = \left(\frac{4\pi m_e c}{3q_e B'} \right)^{1/2} \left(\frac{\nu'}{x} \right)^{1/2} = C_1 \left(\frac{\nu'}{x} \right)^{1/2}$. We assume the distribution of electrons is $dN'_e/d\gamma'_e = C_2 \gamma_e'^{-p}$, then Equation (C2) can be written as

$$\kappa_{\nu'} = \frac{C_0 C_1^{-p} C_2 (p+2)}{16\pi m_e} \left[\int_{x_M}^{\min[x_m, x_c]} x^{(p-2)/2} F(x) dx \right] \nu'^{-(p+4)/2}. \quad (\text{C3})$$

where $x_m = \nu' / \nu'_m$ and $x_M = \nu' / \nu'_M$.

In the slow cooling case,

$$\frac{dN'_e}{d\gamma'_e} = \begin{cases} C_2 \gamma_e'^{-p}, & \gamma'_m \leq \gamma'_e \leq \gamma'_c, \\ C_2 \gamma'_c \gamma_e'^{-p-1}, & \gamma'_c < \gamma'_e \leq \gamma'_M, \end{cases} \quad (\text{C4})$$

the integral in Equation (C3) can be performed for ν' as (also see Wu et al. 2003):

$$\kappa_{\nu'} \simeq \begin{cases} C_2 \frac{8\pi^2}{9} \frac{p+2}{2^{1/3} \Gamma(1/3)} \frac{q_e}{B'} \gamma_m'^{-(p+4)} \left(\frac{\nu'}{\nu'_m} \right)^{-5/3}, & \nu' < \nu'_m, \\ C_2 \frac{\sqrt{3}\pi}{9} 2^{(p+2)/2} \Gamma\left(\frac{p}{4} + \frac{11}{6}\right) \Gamma\left(\frac{p}{4} + \frac{1}{6}\right) \frac{q_e}{B'} \gamma_m'^{-(p+4)} \left(\frac{\nu'}{\nu'_m} \right)^{-(p+4)/2}, & \nu'_m < \nu' < \nu'_c, \\ C_2 \frac{\sqrt{3}\pi}{9} 2^{(p+3)/2} \Gamma\left(\frac{p}{4} + \frac{25}{12}\right) \Gamma\left(\frac{p}{4} + \frac{5}{12}\right) \frac{q_e}{B'} \gamma_m'^{-(p+4)} \left(\frac{\nu'_c}{\nu'_m} \right)^{-(p+4)/2} \left(\frac{\nu'}{\nu'_c} \right)^{-(p+5)/2}, & \nu'_c < \nu' < \nu'_M, \\ C_2 \sqrt{3}\pi \left(\frac{\pi}{2}\right)^{1/2} (p+2) \frac{q_e}{B'} \gamma_m'^{-(p+4)} \left(\frac{\nu'_c}{\nu'_m} \right)^{-(p+4)/2} \left(\frac{\nu'_M}{\nu'_c} \right)^{-(p+5)/2} \left(\frac{\nu'}{\nu'_M} \right)^{-5/2} e^{-\nu'/\nu'_M}, & \nu' > \nu'_M, \end{cases} \quad (\text{C5})$$

where $\Gamma(p)$ is the Gamma function. In the fast cooling case,

$$\frac{dN'_e}{d\gamma'_e} = \begin{cases} C_2 \gamma_e'^{-2}, & \gamma'_c \leq \gamma'_e \leq \gamma'_m, \\ C_2 \gamma_m'^{p-1} \gamma_e'^{-p-1}, & \gamma'_m < \gamma'_e \leq \gamma'_M, \end{cases} \quad (\text{C6})$$

the integral in Equation (C3) gives:

$$\kappa_{\nu'} \simeq \begin{cases} C_2 \frac{4\pi^2}{3} \frac{q_e}{B'} \gamma_c'^{-6} \left(\frac{\nu'}{\nu'_c} \right)^{-5/3}, & \nu' < \nu'_c, \\ C_2 \frac{4\sqrt{3}\pi}{9} \Gamma\left(\frac{14}{6}\right) \Gamma\left(\frac{2}{3}\right) \frac{q_e}{B'} \gamma_c'^{-6} \left(\frac{\nu'}{\nu'_c} \right)^{-3}, & \nu'_c < \nu' < \nu'_m, \\ C_2 \frac{\sqrt{3}\pi}{9} 2^{(p+3)/2} \Gamma\left(\frac{p}{4} + \frac{25}{12}\right) \Gamma\left(\frac{p}{4} + \frac{5}{12}\right) \frac{q_e}{B'} \gamma_c'^{-6} \left(\frac{\nu'_m}{\nu'_c} \right)^{-3} \left(\frac{\nu'}{\nu'_m} \right)^{-(p+5)/2}, & \nu'_m < \nu' < \nu'_M, \\ C_2 \sqrt{3}\pi \left(\frac{\pi}{2}\right)^{1/2} (p+2) \frac{q_e}{B'} \gamma_c'^{-6} \left(\frac{\nu'_m}{\nu'_c} \right)^{-3} \left(\frac{\nu'_M}{\nu'_m} \right)^{-(p+5)/2} \left(\frac{\nu'}{\nu'_M} \right)^{-5/2} e^{-\nu'/\nu'_M}, & \nu' > \nu'_M. \end{cases} \quad (\text{C7})$$

REFERENCES

- Antonelli, L. A., D’Avanzo, P., Perna, R., et al. 2009, *A&A*, 507, L45
- Beloborodov, A. M., & Uhm, Z. L. 2006, *ApJL*, 651, 1
- Berger, E., Kulkarni, S. R., Pooley, G., et al. 2003, *Nature*, 426, 154
- Blandford, R. D., & McKee, C. F. 1976, *Physics of Fluids*, 19, 1130
- Blandford, R. D., & Znajek, R. L. 1977, *MNRAS*, 179, 433
- Blumenthal, G. R., & Gould, R. J. 1970, *Reviews of Modern Physics*, 42, 237
- Burrows, D. N., Hill, J. E., Nousek, J. A., et al. 2005, *Space Sci. Rev.*, 120, 165
- Curran, P. A., Evans, P. A., de Pasquale, M., Page, M. J., & van der Horst, A. J. 2010, *ApJL*, 716, 135
- Dai, Z. G. 2004, *ApJ*, 606, 1000
- Dai, Z. G., & Liu, R. Y. 2012, *ApJ*, 759, 58
- Dai, Z. G., & Lu, T. 1998a, *A&A*, 333, L87
- Dai, Z. G., & Lu, T. 1998b, *Phys. Rev. Lett.*, 81, 4301
- Dai, Z. G., & Lu, T. 1999, *ApJL*, 519, 155
- Dai, Z. G., Wang, X. Y., Wu, X. F., & Zhang, B. 2006, *Science*, 311, 1127
- Dai, Z. G., & Wu, X. F. 2003, *ApJL*, 591, 21
- De Pasquale, M., Kuin, N. P. M., Oates, S., et al. 2015, *MNRAS*, 449, 1024
- Fan, Y., & Piran, T. 2006, *MNRAS*, 369, 197
- Fan, Y.-Z., & Xu, D. 2006, *MNRAS*, 372, L19
- Filgas, R., Greiner, J., Schady, P., et al. 2012, *A&A*, 546, A101
- Filgas, R., Krühler, T., Greiner, J., et al. 2011, *A&A*, 526, A113
- Foreman-Mackey, D., Hogg, D. W., Lang, D., & Goodman, J. 2013, *PASP*, 125, 306
- Gat, I., van Eerten, H., & MacFadyen, A. 2013, *ApJ*, 773, 2
- Gehrels, N., Chincarini, G., Giommi, P., et al. 2004, *ApJ*, 611, 1005
- Geng, J. J., Wu, X. F., Huang, Y. F., & Yu, Y. B. 2013, *ApJ*, 779, 28

- Geng, J. J., Wu, X. F., Li, L., Huang, Y. F., & Dai, Z. G. 2014, *ApJ*, 792, 31
- Granot, J., Piran, T., & Sari, R. 1999, *ApJ*, 513, 679
- Greiner, J., Krühler, T., Nardini, M., et al. 2013, *A&A*, 560, A70
- He, H.-N., Wang, X.-Y., Yu, Y.-W., & Mészáros, P. 2009, *ApJ*, 706, 1152
- Heger, A., Fryer, C. L., Woosley, S. E., Langer, N., & Hartmann, D. H. 2003, *ApJ*, 591, 288
- Hou, S. J., Geng, J. J., Wang, K., et al. 2014, *ApJ*, 785, 113
- Huang, Y. F., Dai, Z. G., & Lu, T. 1999, *MNRAS*, 309, 513
- Huang, Y. F., Gou, L. J., Dai, Z. G., & Lu, T. 2000, *ApJ*, 543, 90
- Huang, Y.-F., Lu, Y., Wong, A. Y. L., & Cheng, K. S. 2007, *Chin. J. Astron. Astrophys.*, 7, 397
- Huang, Y. F., Wu, X. F., Dai, Z. G., Ma, H. T., & Lu, T. 2004, *ApJ*, 605, 300
- Kong, S. W., Wong, A. Y. L., Huang, Y. F., & Cheng, K. S. 2010, *MNRAS*, 402, 409
- Kumar, P., & Zhang, B. 2015, *Phys. Rep.*, 561, 1
- Lan, M.-X., Wu, X.-F., & Dai, Z.-G. 2016, *ApJ*, submitted, arXiv:1602.07497
- Laskar, T., Berger, E., Margutti, R., et al. 2015, *ApJ*, 814, 1
- Lazzati, D., Rossi, E., Covino, S., Ghisellini, G., & Malesani, D. 2002, *A&A*, 396, L5
- Lei, W.-H., Zhang, B., & Liang, E.-W. 2013, *ApJ*, 765, 125
- Lemoine, M., & Pelletier, G. 2003, *ApJ*, 589, L73
- Levesque, E. M., Bloom, J. S., Butler, N. R., et al. 2010, *MNRAS*, 401, 963
- Li, L., Liang, E.-W., Tang, Q.-W., et al. 2012, *ApJ*, 758, 27
- Liang, E.-W., Li, L., Gao, H., et al. 2013, *ApJ*, 774, 13
- Liu, Xue-Wen, Wu, Xue-Feng, & Lu, Tan, 2010, *ScChG*, 53, 262
- Lu, R.-J., Wei, J.-J., Qin, S.-F., & Liang, E.-W. 2012, *ApJ*, 745, 168
- Lü, H.-J., & Zhang, B. 2014, *ApJ*, 785, 74
- Lyubarsky, Y., & Kirk, J. G. 2001, *ApJ*, 547, 437
- MacFadyen, A. I., & Woosley, S. E. 1999, *ApJ*, 524, 262
- Melandri, A., Virgili, F. J., Guidorzi, C., et al. 2014, *A&A*, 572, A55

- Mészáros, P., & Rees, M. J. 1997, *ApJ*, 476, 232
- Metzger, B. D., Giannios, D., Thompson, T. A., Bucciantini, N., & Quataert, E. 2011, *MNRAS*, 413, 2031
- Metzger, B. D., & Piro, A. L. 2014, *MNRAS*, 439, 3916
- Nardini, M., Elliott, J., Filgas, R., et al. 2014, *A&A*, 562, A29
- Nardini, M., Greiner, J., Krühler, T., et al. 2011, *A&A*, 531, A39
- Nicuesa Guelbenzu, A., Klose, S., Rossi, A., et al. 2011, *A&A*, 531, L6
- Panaitescu, A., Mészáros, P., Burrows, D., et al. 2006, *MNRAS*, 369, 2059
- Panaitescu, A., & Vestrand, W. T. 2011, *MNRAS*, 414, 3537
- Pe’er, A. 2012, *ApJL*, 752, 8
- Piran, T. 1999, *Phys. Rep.*, 314, 575
- Piran, T., Shemi, A., & Narayan, R. 1993, *MNRAS*, 263, 861
- Porth, O., Komissarov, S. S., & Keppens, R. 2013, *MNRAS*, 431, L48
- Ramirez-Ruiz, E., Celotti, A., & Rees, M. J. 2002, *MNRAS*, 337, 1349
- Rees, M. J., & Gunn, J. E. 1974, *MNRAS*, 167, 1
- Ryan, G., van Eerten, H., & MacFadyen, A. 2013, arXiv:1307.6334
- Rybicki, G. B., & Lightman, A. P. 1979, *Radiative Processes in Astrophysics* (New York: Wiley-Interscience)
- Sari, R., & Piran, T. 1999, *ApJ*, 520, 641
- Shapiro, S. L., & Teukolsky, S. A. 1983, *Research Supported by the National Science Foundation* (New York: Wiley-Interscience), p. 663
- Uhm, Z. L. 2011, *ApJ*, 733, 86
- Uhm, Z. L., Zhang, B., Hascoët, R., et al. 2012, *ApJ*, 761, 147
- van Eerten, H. 2014, *MNRAS*, 442, 3495
- van Eerten, H. J. 2015, *J. High Energy Astrophys.*, 7, 23
- van Eerten, H. J., Meliani, Z., Wijers, R. A. M. J., & Keppens, R. 2009, *MNRAS*, 398, L63
- Waxman, E. 1997, *ApJL*, 491, 19

- Woosley, S. E. 1993, *ApJ*, 405, 273
- Wu, X. F., Dai, Z. G., Huang, Y. F., & Lu, T. 2003, *MNRAS*, 342, 1131
- Xin, L.-P., Liang, E.-W., Wei, J.-Y., et al. 2011, *MNRAS*, 410, 27
- Xue, R.-R., Fan, Y.-Z., & Wei, D.-M. 2009, *A&A*, 498, 671
- Yu, Y. W., & Dai, Z. G. 2007, *A&A*, 470, 119
- Yu, Y. B., Huang, Y. F., Wu, X. F., Xu, M., & Geng, J. J. 2015, *ApJ*, 805, 88
- Yu, Y. W., Liu, X. W., & Dai, Z. G. 2007, *ApJ*, 671, 637
- Zhang, B., Fan, Y. Z., Dyks, J., et al. 2006, *ApJ*, 642, 354
- Zhang, B., & Kobayashi, S. 2005, *ApJ*, 628, 315
- Zhang, B., & Mészáros, P. 2002, *ApJ*, 566, 712
- Zhang, W., & MacFadyen, A. 2009, *ApJ*, 698, 1261

Table 1. A brief summary of the observed features of the four GRBs.

Observational Characteristics	GRB 080413B	GRB 090426	GRB 091029	GRB 100814A
Duration (s)	8.0 ± 1.0	1.28 ± 0.09	39.2 ± 5	174.5 ± 9.5
z	1.1	2.609	2.752	1.44
$E_{\gamma, \text{iso}}^{\text{a}}$ (10^{52} erg)	1.8	$\simeq 0.42$	8.3	$\simeq 7$
$T_{\text{peak},1}^{\text{b}}$ (s)	~ 90	~ 100	400	~ 300
$T_{\text{peak},2}^{\text{c}}$ (s)	~ 7000	$\sim 10^4$	$\sim 10^4$	$\sim 10^5$
Reference	1	2,3	4	5

^a $E_{\gamma, \text{iso}}$ is the energy released in the prompt phase.

^b $T_{\text{peak},1}$ is the time of the early peak in the optical light curves.

^c $T_{\text{peak},2}$ is the peak time of the re-brightening in the optical light curves.

Note. — Strictly speaking, $T_{\text{peak},1}$ should be the time of the early peak appearing in the light curve. However, the peak may not be captured if the ground-based telescopes do not respond quickly enough. In this case, we set $T_{\text{peak},1}$ to be roughly the time of the first observational data.

References. — (1) Filgas et al. (2011); (2) Levesque et al. (2010); (3) Nicuesa Guelbenzu et al. (2011); (4) Filgas et al. (2012); (5) De Pasquale et al. (2015).

Table 2. Parameters used in the fit of the afterglows of the four GRBs.

Parameters	GRB 080413B	GRB 090426	GRB 091029	GRB 100814A
$E_{K, \text{iso}}$ (10^{52} erg)	5.0	4.0	8.0	7.0
Γ_0	400	300	200	150
θ_j (rad)	0.09	0.08	0.06	0.058
p_2	2.05	2.5	2.2	2.1
$\epsilon_{e,2}$	0.045	0.015	0.007	0.023
$\epsilon_{B,2}$	0.015	0.001	0.5	0.05
B_{NS} (10^{14} G)	1.9	5.0	5.5	1.6
Γ_4 (10^4)	4.0	1.0	50.0	20.0
p_3	2.8	2.5	2.3	2.45
$\epsilon_{B,3}$	0.2	0.001	0.3	0.18
n_1 (cm^{-3})	0.1	50.0	0.02	0.1
$\chi^2/\text{d.o.f.}$	7.5	4.9	11.6	20.7

Note. — The relatively high $\chi^2/\text{d.o.f.}$ of GRB 100814A is due to the bad fitting to the data of g-band. This is the shortness of our model since our model is only good at interpreting the data of which the spectrum is strictly a broken-power-law. When we apply our model to the data with one or two bands deviating from the power-law determined by the data of the rest bands, we would get high $\chi^2/\text{d.o.f.}$.

Table 3. Parameters constrained from the fit of the afterglows of the four GRBs.

Parameters	GRB 080413B	GRB 090426	GRB 091029	GRB 100814A
B_{NS} (10^{14} G)	$1.73^{+0.03}_{-0.03}$	$5.29^{+0.14}_{-0.16}$	$5.81^{+0.14}_{-0.04}$	$1.44^{+0.04}_{-0.01}$
Γ_4 (10^4)	$3.91^{+0.91}_{-0.61}$	$1.07^{+0.61}_{-0.33}$	$81.5^{+7.1}_{-26.7}$	$21.4^{+2.8}_{-1.7}$
$\epsilon_{B,3}$	$0.197^{+0.066}_{-0.052}$	$9.77^{+2.35}_{-2.15} \times 10^{-4}$	$0.35^{+0.07}_{-0.05}$	$0.22^{+0.03}_{-0.03}$

Note. — Limited by the computer resources, we performed the fitting by setting only three parameters as free parameters, but with other parameters fixed as constants taken from Table 2. These three parameters, i.e., B_{NS} , Γ_4 and $\epsilon_{B,3}$, are more interesting since they are directly related with the re-brightening.

¹http://www.swift.ac.uk/xrt_curves/00431605/

²http://www.swift.ac.uk/xrt_curves/309111

³http://www.swift.ac.uk/xrt_curves/350479

⁴http://www.swift.ac.uk/xrt_curves/374210

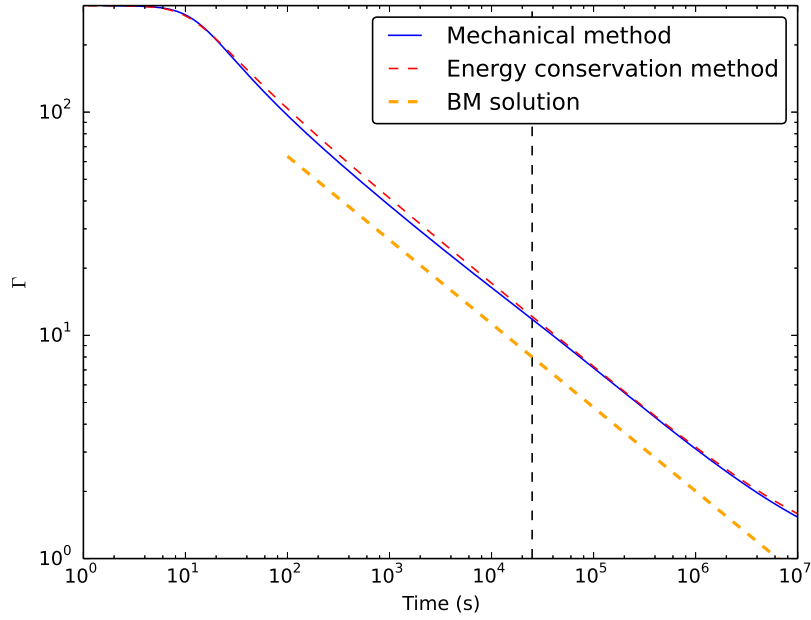


Fig. 1.— Temporal evolution of the bulk Lorentz factor Γ . The blue solid line is the result from the mechanical method and the red dashed line is the result from the energy conservation method. In both cases, the initial parameter values are: $E_{K,\text{iso}} = 1.0 \times 10^{53}$ erg, $\Gamma_0 = 300$, $n_1 = 1 \text{ cm}^{-3}$, $\Gamma_4 = 10^4$, and $B_{\text{NS}} = 2 \times 10^{14}$ G. The thick dashed orange line represents the BM solution (schematic), i.e., $\Gamma \propto t_{\text{obs}}^{-3/8}$ and the vertical dashed line denotes the time of T_{sd} .

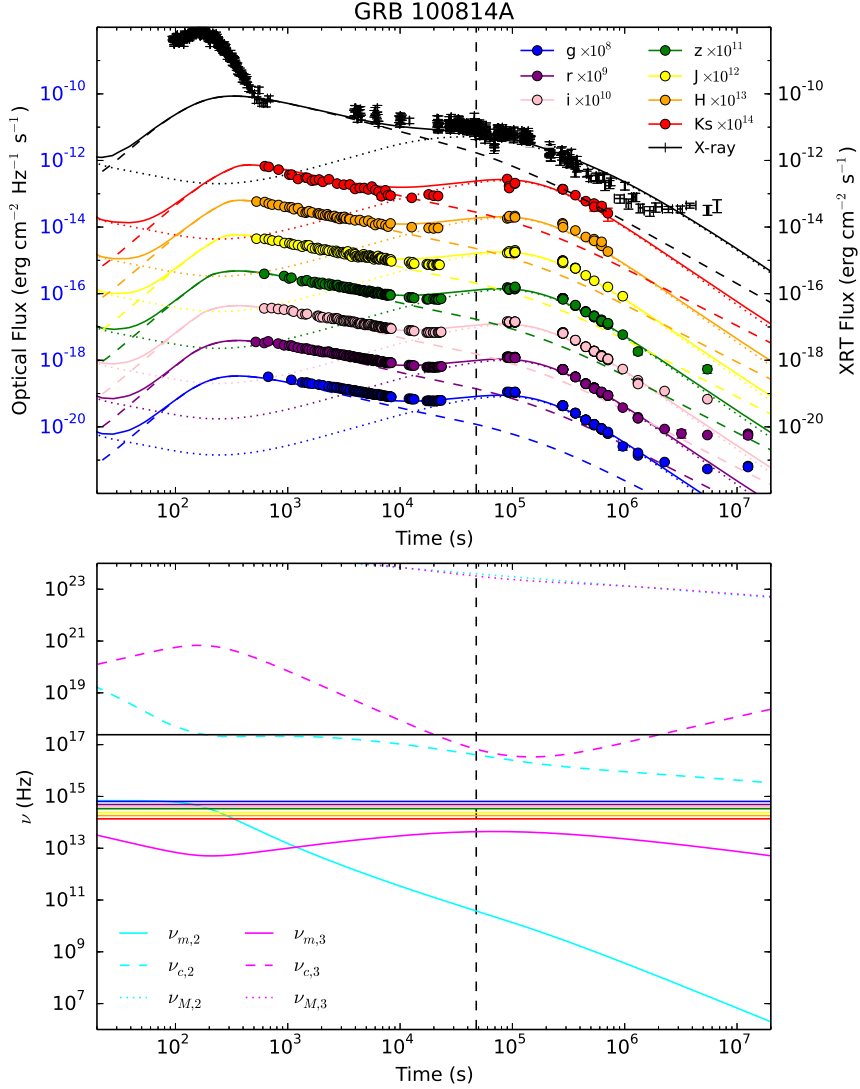


Fig. 2.— Fitting to the multi-wavelength afterglow of GRB 100814A by using our e^+e^- wind injection model. The upper panel shows the fitting results in seven optical–infrared bands (fluxes at different bands have been multiplied by different factors for clarity). The optical–infrared observational data are taken from Nardini et al. (2014), and the X-ray (0.3–10 keV) data are taken from the *Swift*/XRT website¹. The dashed and dotted lines are emissions from the FS (Region 2) and the RS (Region 3) respectively. The solid lines are the total flux. The vertical dashed line denotes the time of T_{sd} . The lower panel shows the evolution of ν_m (solid lines), ν_c (dashed lines), and ν_M (dotted lines) in Region 2 (cyan color) and Region 3 (magenta color). The horizontal lines represent the effective frequencies of seven optical–infrared bands and the X-ray band (1 keV) respectively.

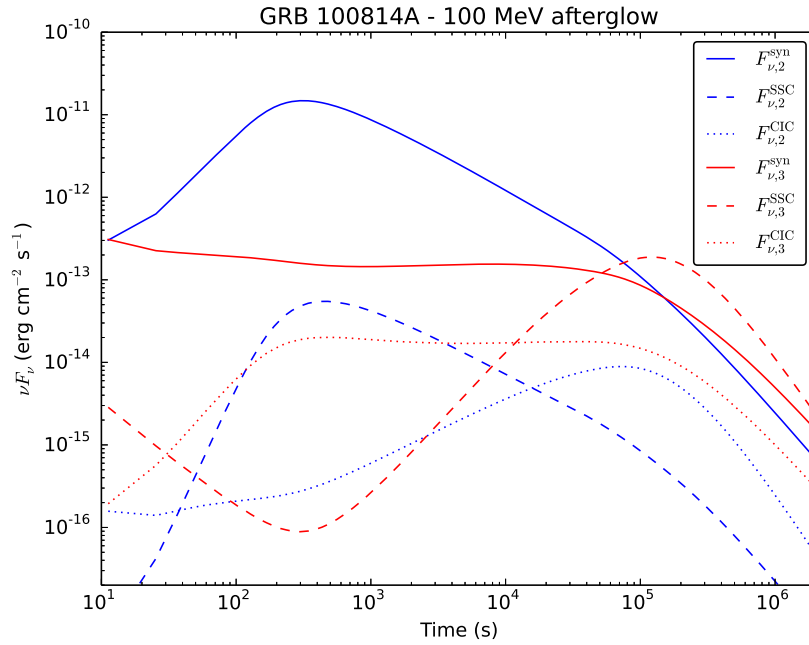


Fig. 3.— High energy emission (at 100 MeV) of GRB 100814A calculated from our model. The parameter values are the same as those in Figure 2. The solid lines represent the synchrotron flux, the dashed lines represent the SSC flux and the dotted lines represent the CIC flux. The blue color denotes the flux from the FS and the red color denotes the flux from the RS.

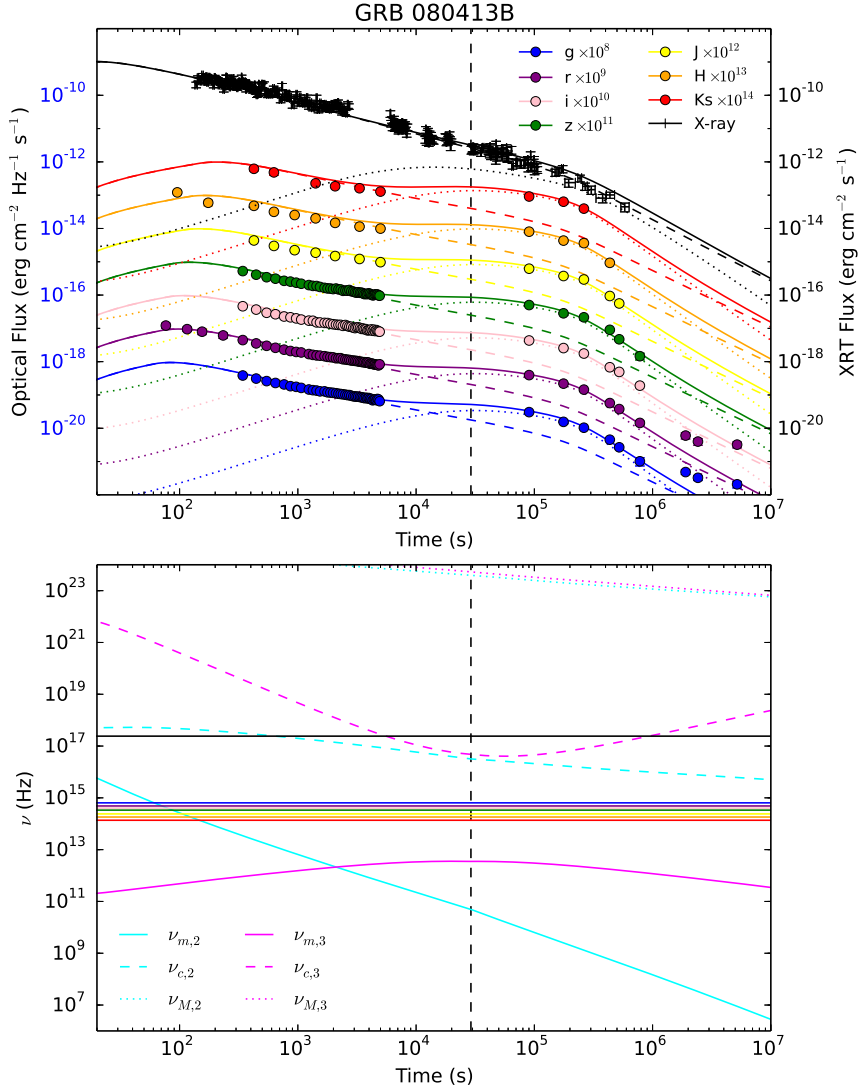


Fig. 4.— Fitting to the multi-wavelength afterglow of GRB 080413B by using our e^+e^- wind injection model. In the upper panel, the optical–infrared observational data are taken from Filgas et al. (2011), and the X-ray (0.3–10 keV) data are taken from the *Swift*/XRT website². The dashed and dotted lines are emissions from the FS and the RS respectively, and the solid lines are the total flux. Detailed fitting parameters are listed in Table 2. Similar to Figure 2, the lower panel shows the evolution of some characteristic frequencies.

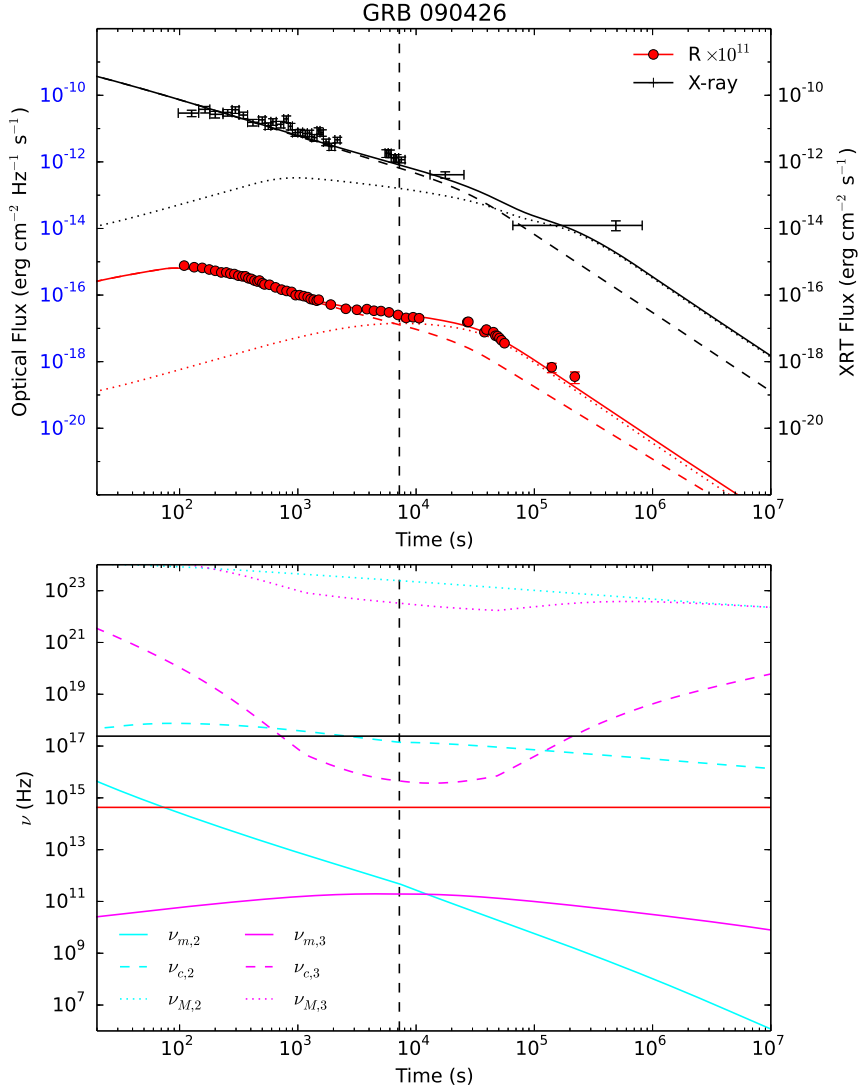


Fig. 5.— Fitting to the multi-wavelength afterglow of GRB 090426 by using our e^+e^- wind injection model. In the upper panel, the observational data in R band are taken from Nicuesa Guelbenzu et al. (2011), and the X-ray (0.3–10 keV) data are taken from the *Swift*/XRT website³. The dashed and dotted lines are emissions from the FS and the RS respectively, and the solid lines are the total flux. Detailed fitting parameters are listed in Table 2. Similar to Figure 2, the lower panel shows the evolution of some characteristic frequencies.

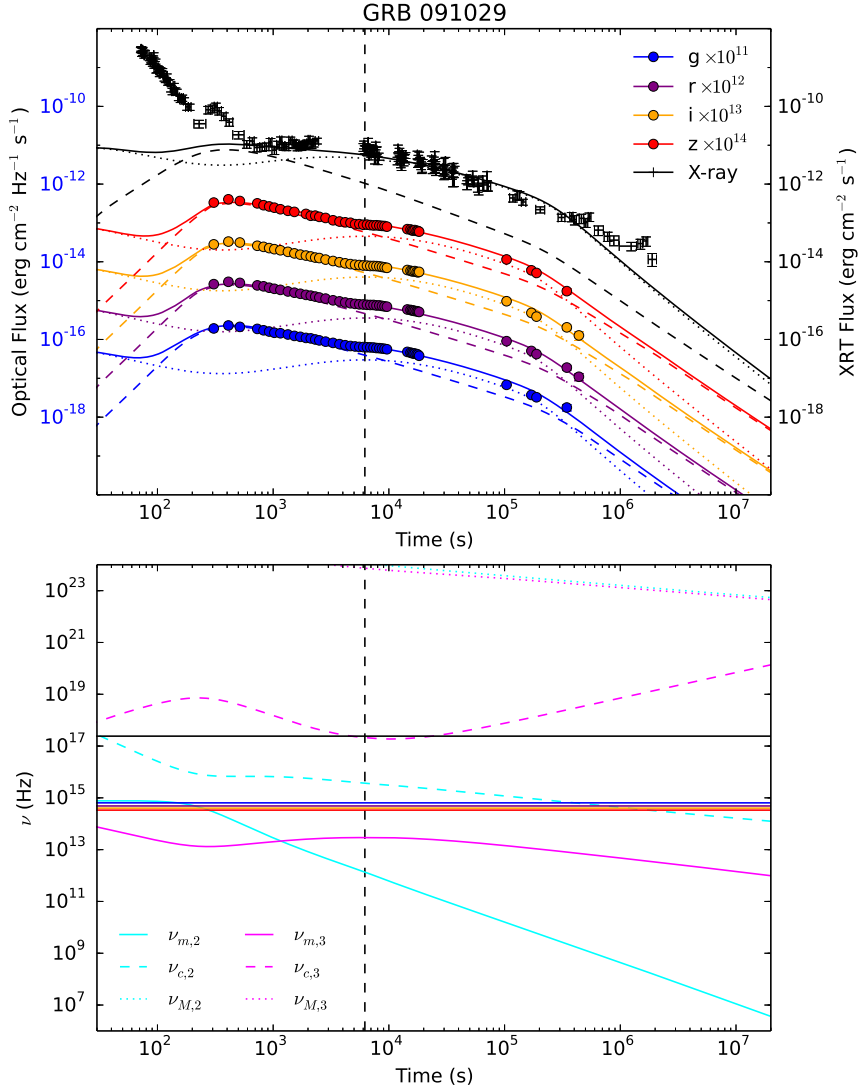


Fig. 6.— Fitting to the multi-wavelength afterglow of GRB 091029 by using our e^+e^- wind injection model. In the upper panel, the optical–infrared observational data are taken from Filgas et al. (2012), and the X-ray (0.3–10 keV) data are taken from the *Swift*/XRT website⁴. The dashed and dotted lines are emissions from the FS and the RS respectively, and the solid lines are the total flux. Detailed fitting parameters are listed in Table 2. Similar to Figure 2, the lower panel shows the evolution of some characteristic frequencies.

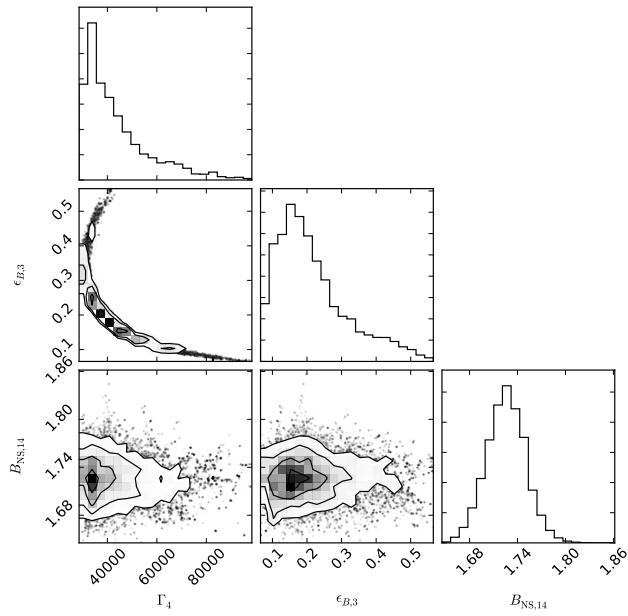


Fig. 7.— The MCMC fitting results for GRB 080413B. The marginalized distribution for each parameter is shown in the histograms along the diagonal. The off-diagonal contour plots show the covariances between various pairs of parameters. Contours are shown at 0.5, 1, 1.5, and 2 sigma. The best-fit values and error bars for parameters in Table 3 are calculated as the median and the 68% credible intervals about the median of the marginalized posterior distribution.

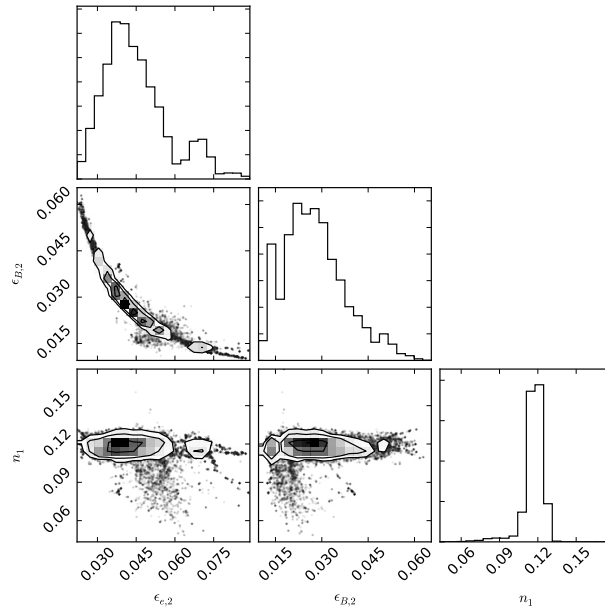


Fig. 8.— Similar to Figure 7 but the free parameters are $\epsilon_{e,2}$, $\epsilon_{B,2}$, n_1 .